Composites Part B 254 (2023) 110577

Contents lists available at ScienceDirect

Composites Part B

journal homepage: www.elsevier.com/locate/compositesb

Fibre volume fraction screening of pultruded carbon fibre reinforced polymer panels based on analysis of anisotropic ultrasonic sound velocity

Euan Duernberger *, Charles MacLeod, Dave Lines

University of Strathclyde, United Kingdom

ARTICLE INFO

Handling Editor: Prof. Ole Thomsen

ABSTRACT

Composites have become the material of choice in a wide range of manufacturing applications. Whilst ultrasound inspection is a well-established non-destructive testing (NDT) technique, the application to composite imaging presents significant challenges stemming from the inherent anisotropy of the material. The fibre-volume fraction (FVF) of a composite plays a key role in determining the final strength and stiffness of a part as well as influencing the ultrasonic bulk velocity.

In this work, a novel FVF determination technique, based on the angular dependence of the sound velocity with respect to the composite fibre direction, is presented. This method is introduced and validated by inspection of pultruded carbon fibre reinforced polymer (CFRP) panels commonly used in the manufacture of high-power wind turbine blades. Full matrix capture (FMC) data acquired from a phased array (PA) ultrasonic probe is used to generate calibration data for samples ranging in FVF from 60.5% to 69.9%. Sample velocity, as a function of propagation angle, is used to estimate the FVF of samples and ensure they fall within the desired range. Experimental results show values of 61.1, 66.1 and 68.3%, comparing favourably to the known values of 60.5, 66.3 and 69.9% respectively.

The work offers significant potential in terms of factory implementation of NDT procedures to ensure final parts satisfy standards and certification by ensuring any FVF inconsistencies are identified as early in the manufacturing process as possible.

1. Introduction

1.1. Composite materials and wind turbine blade design

Composite materials are becoming increasingly prevalent in a variety of engineering and manufacturing applications demanding high-performance materials [1]. A fibre reinforced polymer composite is formed by the combination of load-bearing fibres and a resin matrix, holding these in a fixed structure. These fibres can be made from glass, carbon, or natural materials such as hemp or cotton, and are often arranged in layers with alternating orientations so that the final material's elastic properties are constant in at least one plane. Driving factors behind this shift, away from more traditional metal alloys, are the high modulus and/or strength-to-weight ratio, improved fatigue performance, toughness and durability, as well as the ability to construct complex-geometry parts from fewer individual sections [2,3]. The aerospace industry has been key in developing the manufacture of such materials as well as their application into high-value components that fulfil stringent structural integrity and safety standards [4,5].

Whilst composite materials were pioneered in aerospace, before spreading to automotive and marine applications, they are now also key in the rapidly growing renewables sector. The best example of this being in wind turbine blade construction. Renewable energy targets set by numerous European governments mean that the size of installed wind capacity will continue to grow exponentially over the coming years [6]. As of 2020, wind energy accounted for 24% of total electricity generation in the UK with a roughly even split between onshore and offshore installations [7]. It is predicted that nearly 40 GW installed capacity will be necessary by 2030 if the UK is to meet its legally binding targets of net zero greenhouse gas emissions by 2050 [7–9].

Modern wind turbine blades are manufactured using a combination of both glass and carbon fibre reinforced polymer (GFRP and CFRP) and possess complex geometries, aerodynamically optimised to simultaneously increase efficiency, and reduce loading on the structure. Whilst the root is optimised for strength, sections further from the hub are designed primarily for aerodynamic efficiency [10]. Wind-turbine

* Corresponding author.
E-mail addresses: euan.duernberger@strath.ac.uk (E. Duernberger), charles.macleod@strath.ac.uk (C. MacLeod), dave.lines@strath.ac.uk (D. Lines).

https://doi.org/10.1016/j.compositesb.2023.110577
Received 31 August 2022; Received in revised form 19 January 2023; Accepted 27 January 2023
Available online 2 February 2023

blades are now approaching 100 m in length with nameplate capacities exceeding 8–10 MW per turbine [11,12]. During blade manufacture, additional strength and stiffness is often given to GFRP main aerofoil sections using two beams running up the centre of the structure. These beams are manufactured from pultruded CFRP panels and subsequently incorporated into the glass fibre layup process as shown in Fig. 1. Pultrusion is a low maintenance process where carbon fibres are saturated as they are pulled through a resin bath. The result is a single-ply panel. Similar components are also found as reinforcement in steel and concrete structures [13,14].

1.2. Fibre volume fraction

The fibre volume fraction is the percentage of the composite taken up by the fibres and typically in the range of 50–70%. From a geometric analysis, FVFs higher than 90% are impossible, due to the gaps occupied by resin, even if fibres are arranged in a triangular sequence, achieving the maximum FVF. A square stacking gives a maximum of 78% and both these cases are illustrated in Fig. 2. In practice even this is difficult to achieve with values higher than 70% not commonly found in unidirectional fibre composites [1].

The practically achievable FVF is dependent on this fibre architecture as well as the method of manufacture, principally the pressure applied during the curing process, with typical CFRP laminates having FVFs around 60%. Investigations of achievable FVF for both woven and unidirectional fibres using no consolidation pressure, vacuum infusing and high-pressure autoclave treatment, found that only with unidirectional fibres, in the form of plies or simple pultrusion, and 5–7 bar autoclave infusion could FVFs in the 60–80% range be achieved [15].

FVF is one parameter key in understanding the mechanical properties of carbon composites [15–17]. Effect of FVF on stiffness and strength, fracture toughness, typical damage mechanisms, as well as their evolution, are detailed in Refs. [15,18–21]. A FVF of 60–70% in CFRP has been shown to result in optimal mechanical properties [22]. This was demonstrated for an automotive application in the design of a composite suspension in Ref. [15]. Increasing the FVF from 40% to 70%, yielded a linear relationship between tensile properties. A greater FVF, within this range, giving a greater strength in the final composite material since the fibre strength is greater than that of the matrix material. However, beyond 70% there was decrease in the strength owing to insufficient resin to wet the fibres producing a more brittle part [15].

FVF is commonly determined through destructive means. This can be achieved by measuring the weight of a small sample before and after burning the resin away using acid digestion [23]. The sample is exposed to a highly oxidising acid, at elevated temperature, until the resin matrix has completely dissolved. FVF determination is then a case of weighing the remaining fibres and expressing this a proportion of the total composite volume [24,25]. The most common chemistry used for composites of this type are polyesters, vinyl esters, polyurethane, and epoxies. These substances are usually very inert towards most solvents making chemical digestion difficult. The industry standard, ASTM D3171-22, to determine FVF, is based on this method [26]. After digestion, ignition, or carbonization, by one of eight procedures, the fibres are essentially unaffected. This allows for calculation of weight and volume of both

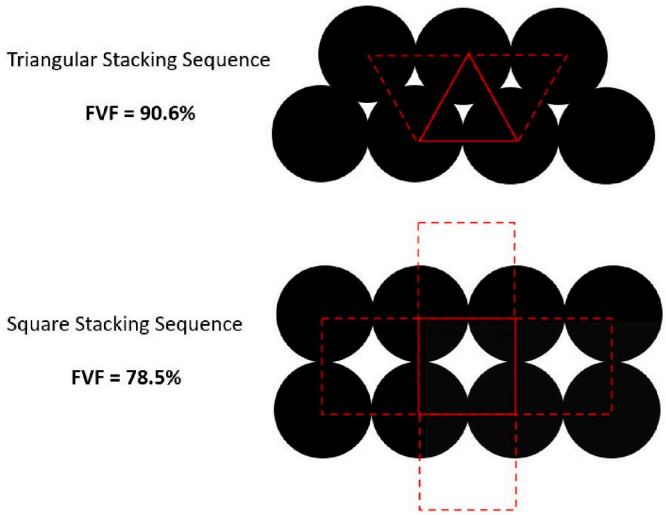

Fig. 2. Schematic giving a cross-sectional view of composite fibres with geometry calculations yielding maximum FVFs.

constituents. Using the composite density compared to these volume fractions also yields the void content and the level of porosity as a percentage [27]. The standard details a second method, applicable only to laminate materials of known fibre weight, and calculates reinforcement or matrix content using the thickness of the laminate [26].

Conventional FVF measurement is a form of destructive testing and possesses inherent drawbacks. Firstly, it is time-consuming, thus making it completely unfeasible to integrate seamlessly into a manufacturing workflow. Resin burn-off typically takes one day of preparation before the testing can be carried out. Acid digestion is an even longer process taking two days until only the composite fibres remain. Both methods involve hazardous chemicals, bringing with them additional safety concerns and procedures. For glass fibres, digestion can be performed in one step. However destructive FVF measurement of carbon fibre composites requires two distinct stages. Step one is carried out within an inert atmosphere where the matrix is degraded to carbon ash. The second step performed in air, is to remove this residual ash. Regardless of which method chosen, it is challenging to take additives or fillers into account. FVF can only be determined precisely if the exact content of these is known.

Alternatives exist and are described in Refs. [16,28–30]. These include optical microscopy or the use of carbonization instead of acid digestion. The result of carbonization is the same, in that only the fibres remain for weight and volume determination. Optical microscopy-based techniques allow for the FVF to be determined by image analysis but again this is a destructive technique and involves cutting a section of sample. These methods are also time consuming, and in most cases, only take a small sample size into account, thereby reducing confidence levels across a larger component.

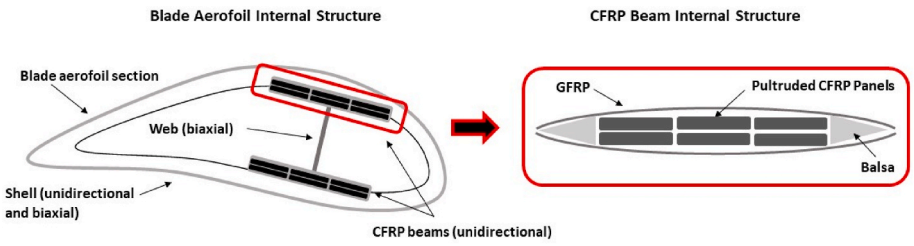

Fig. 1. Schematic of wind turbine blade internal structure and use of pultruded CFRP panels in structural beam.

1.3. Ultrasonic NDT

Non-destructive testing (NDT) is an important stage of any manufacturing process and ultrasonic inspection is a commonly used technique used to analyse the interior structure of a component. Ultrasound refers to any sound waves beyond the 20 kHz limit of human hearing. In NDT, sound frequencies in the range of 100 kHz to 20 MHz are used, depending on the sample material and type of inspection [31]. It is particularly attractive as a NDT technique due to reliability, volumetric inspection capability and a proven track record [32–34]. Ultrasonic NDT has its advantages over other methods such a thermography, acoustic emission and shearography, when applied to composites. These include good resolution, flaw detection capabilities, as well as the ability of in-situ usage [35]. Using signal processing techniques information regarding the geometry, material characteristics or presence of any defects within can be acquired, allowing the user to build a highly accurate representation of an object [36,37]. The current state of NDT applied to composite wind turbine blades both at the manufacturing stage and once in service has been reviewed in detail in Refs. [38–40].

Ultrasonic inspection can be carried out using single element transducers or by phased array ultrasound testing (PAUT) [41]. Phased arrays contain many individual piezoelectric transducers, arranged in a linear or matrix fashion. These can be individually addressed in both transmission and reception with programmable differential time-delays allowing the resulting ultrasound beams to be steered to, and focussed at, specific locations [42]. Phased arrays can facilitate beam movement electronically without the need to mechanically move the array. A, B and C scans are the fundamental ultrasound data presentation formats, key to understanding general ultrasound imaging and the characterisation of features. An A-scan displays the amount of energy received as a function of time, the basis for more complex imaging. B and C-scans are two-dimensional representations showing the cross-sectional or plan-view of a parameter, respectively. Defect detection capabilities are also enhanced using PAUT. A variety of imaging modalities and post-processing algorithms exist, which are not applicable to single-element probes [43]. For example, full-matrix capture (FMC) collects data from every reception channel, whilst firing each element in turn, resulting in a matrix of all possible transmission and reception combinations. This allows for decoupling of the acquisition and reconstruction stages [44,45]. One example of an imaging technique applied to FMC data is the total focussing method (TFM). This employs time delays, based on sample geometry and ultrasonic velocity, to give an image in which every point is in focus.

The TFM method can also be applied to composites. However, ray tracing and imaging algorithms must account for the angular dependence of ultrasound velocity. If this inherent anisotropy is not considered, then defects can be missed, or their location incorrectly identified [46,47]. The velocity has a strong dependence on the angle made to the composite plies and therefore the TFM algorithm must be modified to include this direction-dependent velocity profile [3]. Anisotropy can also cause issues in ultrasonic imaging of metals. Anisotropic stiffness maps have been shown to result in significant improvements in ultrasonic inspection of welds in Ref. [48]. A second example of this problem in practice was presented in Ref. [49], where defects in a single crystal titanium alloy could only be imaged to a high standard once material anisotropy was accounted for.

1.4. Contributions to knowledge and layout

In this work, a novel method to determine the FVF of CFRP panels, used in wind turbine blade construction, is introduced, developed, and validated experimentally. In its current form, the method is intended as a screening technique, during manufacture and assembly, to ensure the FVF falls within a desired range and thus the mechanical properties of the material are consistent. It is shown that ultrasonic velocity, as a function of propagation angle, is a reliable and repeatable measurement parameter that can give accurate estimates of FVF. Thereby, the anisotropic nature of CFRP is exploited to allow one to distinguish between samples of varying FVFs.

A phased array transducer acquiring FMC data, enables time of flight measurement across a range of transmit and receive elements, giving angular variation with respect to the fibres, used to generate calibration curves. Validation tests can then be carried out, compared to these calibration curves, and estimates of FVF generated. The data volume required for this procedure is minimal and thus could be implemented as part of a conventional ultrasonic inspection, without significant impact on the frame rate and consequent inspection resolution or scan speed. At this stage, the focus is on the reliability and repeatably of FVF determination rather than the absolute quantitative values. This is with a view to application as a screening process in the manufacturing environment.

The paper is structured as follows: The introductory section has highlighted the increased use of composite materials and reviewed the current methods of FVF measurement as well and the effect of this parameter on mechanical properties. A background to ultrasonic measurement and NDT of composites has also been given. Next, the mathematical theory behind ultrasonic FVF measurement is detailed in Section 2. This includes a ray propagation model, on which the calculation of effective velocity as a function of angle made to the fibres is based. The hardware used is outlined in Section 3 and includes relevant inspection parameters. Alongside practical work, computer simulation is also carried out in Section 4. Results are presented in Section 5 and the paper concludes with discussions, recommendations for improvement, as part of any future work, and a conclusion.

2. Ultrasonic FVF measurement theory

A brief introduction to the sample and ultrasonic inspection hardware is now given. This is necessary at this stage to clarify the parameters referred to in the ultrasonic FVF measurement theory. A more thorough description of CFRP panels inspected and experimental set-up is given later after the measurement theory is detailed. A CFRP sample, from the previously described turbine construction process, Fig. 1, is used to demonstrate the mathematical theory. PAUT is carried out using a self-contained water-delay line and dry-coupling medium to transmit ultrasound into the sample. Fig. 3 shows a schematic of the inspection set-up, parameters of which are referred to in the following paragraphs. The mathematical theory behind the proposed approach for ultrasonic determination of FVF, is based on a ray propagation model of this schematic. The model is applicable to any phased array inspection comprising a delay line, coupling and sample with known thicknesses and ultrasound velocities, with the example shown here using the application presented in this paper.

Similar examples of such models, used to analyse ultrasound data, can be found in literature and applied, for example, to calculate the thickness of a corrosion layer formed after prolonged exposure of the composite in a corrosive environment in Ref. [50]. A calculation is based on sample geometry, probe separation and varying sound velocities. Similarly, a ray propagation model is used along with pulse echo and through transmission data to determine the velocity anisotropy in Ref. [3]. The proposed FVF estimation approach presented here, differs from Ref. [3], in that only one phased array is used, with the transmission and reception apertures acting as the separate transducers. Also, three layers of material are considered and the velocity, as a function of angle in the third layer, the CFRP, is calculated. This angular variation is created by increasing the gap between transmission and reception apertures on the phased array as shown in Fig. 3.

The following paragraphs describe firstly a geometrical analysis of the inspection set up. Distances are known from dimensions and angles calculated to satisfy Snell's law. Next, the time of flight for each stage of the ultrasonic propagation path is expressed in terms of the bulk velocity and the results of the geometrical analysis. This is performed for both the

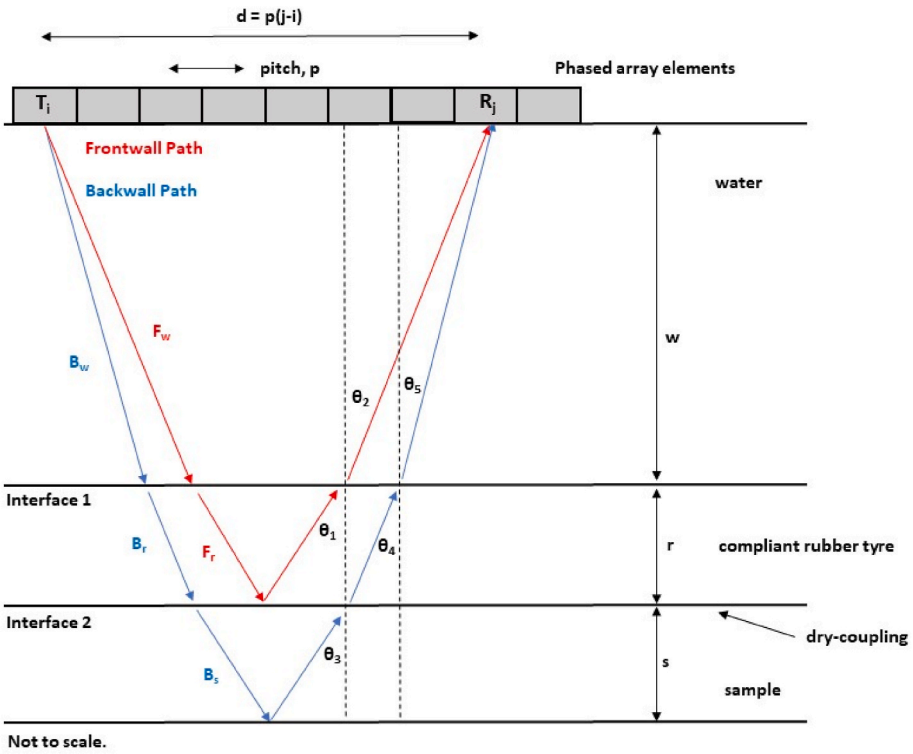

Fig. 3. Schematic illustrating the geometry of wheel probe and sample in a cross-sectional view as well as phased array geometry and the interfaces analysed using Snell's law, for both ray propagation paths.

front wall and back wall propagation paths. The experimental time of flight can be extracted from the corresponding arrival time on each individual A-scan. Combining the geometrical analysis with the time-of-flight data allows for the velocity in the sample, at a certain propagation angle to be isolated.

Two separate acoustic paths corresponding to front and back wall echoes are modelled and analysed. Using the known start and end points of each ray, distances and bulk velocities, Snell's law must be satisfied: $\frac{\sin\theta_1}{v_r} = \frac{\sin\theta_2}{v_w}$ (eq. 1). This yields the refraction points, at each interface. The total time of flight between transmission and reception element is thereby minimised. Refraction angle at interface one is then used as the incident angle at interface two, in Fig. 3. The separate acoustic paths are represented by red and blue lines for front and back wall echo, respectively. Since the velocity influences the ray propagation angles, which in turn are used to calculate the velocity as a function of angle to the plies, the thickness used at the start of the algorithm cannot be dependent on the velocity output. It must be obtained from a separate measurement and used as an input.

The axial distance moved across the array is given by: $\frac{p(j-i)}{2} = rtan\theta_1 + wtan\theta_2 = stan\theta_3 + rtan\theta_4 + wtan\theta_5$ (Eq. 2). Where s, r and t are the thicknesses of sample, dry-coupling medium, and water delay line, respectively. The angles in each medium are defined with respect to the normal. The physical distance along the array, d, between transmission and reception elements is calculated from the number of elements between transmission and reception, (j-i), and the phased array pitch, p.

This calculation is carried out for both the front and back wall propagation path giving an expression for the angles of incidence and refraction as function of the distance shifted across the phased array. The procedure can then be repeated for every transmission and reception combination making up the full FMC matrix. Next, the time delays corresponding to each step of these propagation paths can be computed using the inspection geometry and bulk velocities to yield the following: $F_r = \frac{r}{v_r \cos\theta_1}$, $F_w = \frac{w}{v_w \cos\theta_2}$, $B_s = \frac{s}{v_s \cos\theta_3}$, $B_r = \frac{r}{v_r \cos\theta_4}$, $B_w = \frac{w}{v_w \cos\theta_5}$ (Eq. 3-7).

Variable names are defined such that F_w and B_r correspond to the time delay corresponding to the front wall path in water and back wall path in rubber, respectively. Individual A-scans are extracted from a FMC matrix, the general structure of which shown in Fig. 4.

The time delay, Δt, between front and back wall echo is given by: $\Delta t = \frac{(i_b - i_f)}{f_s}$ (Eq. 8), and illustrated in Fig. 5. Here 'i_b' and 'i_f' refer to the indexed location of the front and backwall peak on each A-scan, with 'f_s' the sampling frequency. This time delay can be expressed in terms of the individual propagation paths, using Eq. 3-7, and yielding: $\frac{\Delta t}{2} = (B_s + B_r + B_w) - (F_r + F_w)$ (Eq. 9).

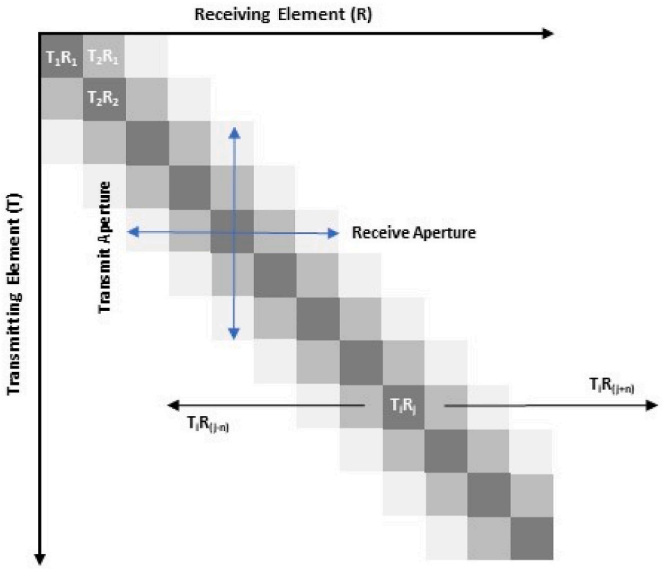

Fig. 4. FMC matrix definition containing A-scans from every possible transmit and receive combination.

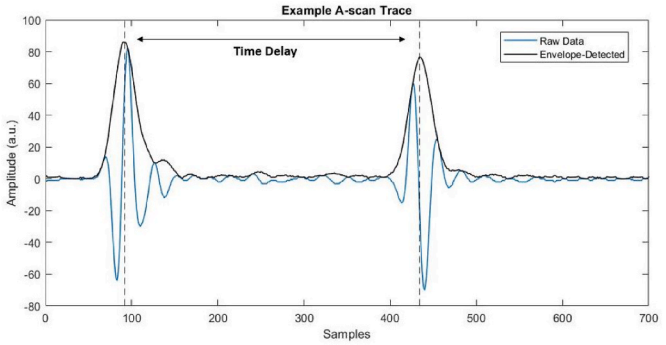

Fig. 5. Example A-scan, highlighting the delay between front and back wall response as well as the envelope detected using the Hilbert Transform.

As is common practice with ToF calculation in various imaging algorithms the arrival time is determined from the Hilbert peak, thereby accounting for both phase and amplitude variation, not the merely RF waveform. Beyond the 1st critical angle, shear wave peaks are recorded alongside longitudinal ones, on each A-scan. The correct front and back wall peak, corresponding to longitudinal waves, must be identified based on amplitude and location relative to the maximum in each scan. Using the propagation path and time delay between front and back wall echo, the speed of sound at angular incidence in the sample, v_s, is isolated. Combining Eq. 3-7with Eq. 9yields the ultrasonic propagation velocity within the sample, v_s, as a function of propagation angle within the sample, θ_3: $v_s(\theta_3) = \left(\frac{\cos\theta_3}{s}\left(\frac{\Delta t}{2} + \frac{r}{v_r \cos\theta_1} + \frac{w}{v_w \cos\theta_2} - \frac{r}{v_r \cos\theta_4} - \frac{w}{v_w \cos\theta_5}\right)\right)^{-1}$ (Eq. 9).

Repeating this procedure across the range of axial distances, A-scan traces in a FMC dataset corresponding to $T_iR_{j\pm25}$, the velocity in the sample as a function of angle shifted from normal propagation is calculated. This generates a cloud of sample velocity values, as a function of propagation angle. Each one corresponding to one A-scan in the FMC matrix. To generate a smooth line from these, a polynomial, of order two, is fitted to the points taken from every ten phased array elements. This is known as a Savitsky-Golay filter, and the curve is shifted incrementally across propagation angles using the corresponding inbuilt MATLAB function.

3. Experimental hardware and CFRP samples

Sample parameters, inspection and phased array geometry are necessary to give the quantitative results to the FVF measurement theory. These samples are flat and planar with a thickness of 5.1 mm and width of 195.5–200.5 mm. They are taken from a full length pultruded CFRP used in wind turbine blade construction, as described in Fig. 1. Such materials are used to construct an internal load bearing beam up to 80 m in length. CFRP panels have FVFs in the range of 60–70%. Exact values are obtained from the supplier, Siemens Gamesa Renewable Energy (SGRE), who conducted both in-house tests, using acid digestion, as well as a third-party FVF measurement. This was carried out by the IMA 'Materialforschung und Anwendungstechnik' in Dresden and in accordance with standard ASTM D3171 Method 1, Procedure B [26,51]. Three separate samples are used in this work with FVFs of 60.5, 66.3 and 69.9%. These values will be referred to as the known values in subsequent sections of this paper.

Phased array ultrasonic testing is carried out using an Olympus 5 MHz, 64-element phased array. The element pitch and height are 0.8 and 10 mm respectively. The fibre diameter is approximately 0.007 mm, with the wavelength from a 5 MHz probe in this composite material around 0.6 mm. This is a difference of three order of magnitude, the material heterogeneity on a scale much smaller than the inspection wavelength. The array is controlled by a PEAK NDT LTPA phased array controller (PAC) supporting 64 channels on both transmission and reception. The self-contained water delay-line and acoustically optimised coupling medium removes the need for liquid coupling, pumping equipment, or immersion tanks, often used in ultrasonic inspection, meaning the risk of water ingress into the sample is negated. Hardware and software are interfaced within the LabVIEW environment. Previous publications have demonstrated the effectiveness of similar set-ups when applied to PAUT of composite aerospace components [52,53]. Table 1 details inspection parameter values referred to in Fig. 3.

To distinguish between panels of different FVFs, using the described ray propagation method, the phased array must be parallel to the fibre orientation. Since angular variation is achieved by increasing the gap between transmission and reception apertures, this must be orientated along the fibre direction, as shown in Fig. 6. It is necessary for the sound to travel along, not across, the fibres so that increasing their number, by increasing FVF, causes an increase in velocity measured. The FVF affects the ultrasonic propagation velocity at varying angles made across the fibres. Since the sample is of pultruded CFPR, essentially only containing one ply, all fibres are orientated in the same axis, thus simplifying the inspection.

4. Ray tracing simulations

To confirm the validity of the FVF determination method, and to generate data to compare experimental results to, several computer simulations are carried out. For this, the CIVA software package is utilised which is based on a combination of ray tracing and FEM analysis. The version used includes the optional FIDEL add-on for inspection simulation of composite materials [54]. This allows the user to insert specific parameters such as, fibre density and thickness as well as resin density and speed of sound, before performing a sample homogenization. Homogenization starts at the ply level, before considering the number of layers and their orientation. This stage is simplified for a pultruded CRRP sample, as studied here. It is in effect one, much thicker, unidirectional ply.

It is thereby possible to generate data from a simulation of the described experimental set-up. CIVA can accurately model the sample geometry, the parameters of a composite material's constituent parts, and the interaction of such a material with an ultrasonic phased array transducer. Simulated FMC data is used in the ultrasonic FVF measurement theory, Section 2, to generate curves of velocity as a function of propagation angle in the sample. These results are shown, and compared to those obtained from experimental data, in the following sections.

5. Results and discussion

5.1. Anisotropic glass block proof of concept

The theory, presented in Section 2, yields a final expression by which the velocity in the sample can be calculated as a function of propagation angle, Eq. 10. Throughout these sections this is used to characterise the FVF of calibration samples and generate estimates of FVF from validation datasets.

Table 1
Numerical values of necessary inspection parameters from Fig. 3.

Variable	Nomenclature	Numerical Value
Water thickness	W	24 mm
Rubber thickness	R	1 mm
Sample thickness	S	5.0–5.3 mm
Water bulk velocity	v_w	1480 ms^{-1}
Rubber bulk velocity	v_r	1560 ms^{-1}
Sample velocity (across fibres)	v_s	Determined by Model
Element pitch	p	0.8 mm
Gap	g	25 elements

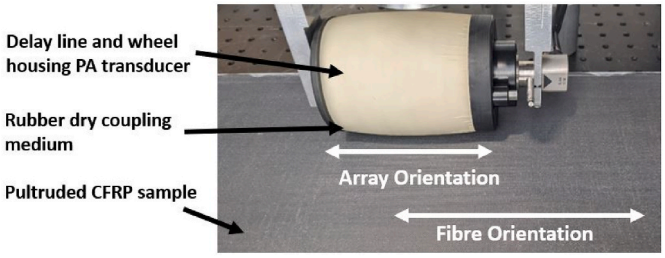

Fig. 6. Image showing the experimental hardware and CFRP sample used, highlighting the necessary array and fibre orientation.

Initially, a proof-of concept, based on FMC data acquired from a isotropic glass calibration block with a thickness of 50 mm, is carried out. Since, anisotropy within CFRP panels is used to distinguish between varying FVFs, this is an important first step. This isotropic sample should generate a straight-line plot of velocity as a function of propagation angle and thereby validate the ray propagation model from Section 2. The sound velocity across a range of angles, by varying transmission and reception elements, is computed and this experimental data, acquired by PAUT, is compared to an equivalent CIVA simulation in Fig. 7.

A straight-line plot of velocity as a function of propagation angle with a constant value of 5915 ms^{-1}, can be seen. At 0°, the same element is utilised for transmission and reception, as in standard pulse-echo inspection. The experimental plot is formed from three separate FMC datasets acquired at various locations on the glass calibration block.

Simulation data from CIVA yields a slightly lesser value of 5912 ms^{-1} with no variation due to the ideal inspection made possible within a computer model. This confirms the isotropic nature of the sample and the validity of the ray tracing algorithm for the next stages of the work. The angular range here is much smaller than in subsequent sections regarding the CFRP panels. This is due to the geometry of the inspection set-up, shown in Fig. 3. The isotopic glass block has a thickness of 50 mm whilst the CFRP panels, 5 mm. All other array and delay line values are identical and thus the same physical gap between transmission and reception element results in an angular range of 0–8° in the glass and 0–31° in the CFRP sample.

5.2. CFRP panel characterisation

Next, three CFRP panels, with known FVFs of 60.5, 66.3 and 69.9% are inspected. These are the calibration samples to which validation data can then be compared. Again, FMC data is acquired experimentally from each and compared to CIVA simulation. The increase in velocity, relative to that found at normal incidence, for each panel is shown in Fig. 8. The normal incidence velocities for FVFs of 60.5, 66.3 and 69.9% are found to be 2877, 2914 and 2958 ms^{-1} respectively.

5.3. Repeatability and mean value curves

For each calibration panel, several datasets were acquired at different locations on the sample. Each is processed to generate a plot of velocity as a function of angle made to the fibres. For each FVF value, an average curve is generated using ten FMC datasets and shown by the solid line in Fig. 9. Again, the velocity relative to that observed at normal incidence for each FVF is plotted. Plus, and minus one, standard deviation curves for each FVF are also shown by the dashed lines. For the purposes of FVF screening, within a manufacturing environment, upper and lower screening limits of one standard deviation above the 69.9% sample and one standard deviation below the 60.5% sample are defined.

5.4. Comparison to conventional measurement

Following the generation of the calibration curves from the average of ten datasets, shown in Fig. 9, a test is carried using a sample of slightly increased thickness, and again known FVF of 60.5%. Fig. 10 shows the velocity as a function of propagation angle, generated from these data, and compared to the average and standard deviation limits provided by the 60.5% FVF calibration sample. The purpose of this step is to prove the validity of the method on different sample geometries and is impactful in that it clearly shows that the velocity as a function of propagation angle is independent of sample thickness.

Next, the method is validated using separate FMC datasets and, by comparison to the screening curves, FVF is determined for each of the three panels. Velocity, at three specific angles, is plotted alongside the calibration curves in Fig. 11, and shown on the graph using crosses for demonstration purposes. This highlights where the data falls on the previous screening curves.

The absolute velocity at each angle, taken from each transmission and reception combination, is then used to produce a FVF estimate. This is achieved by interpolation with the velocity at that angle from the three known FVF curves. A curve of order two is fitted since FVF as a function of velocity does not display a linear increase. Thereby, a FVF estimate is produced at every angle. These values are then averaged to generate a single FVF value from each new dataset. The results generated using this procedure are presented in Table 2 and compared to known values as obtained by acid digestions and carried out by a third party. The method proves effective in the 1–2% discrepancy between the experimental and known values.

Following the generation of the calibration curves from the average of ten datasets, shown in Fig. 9, a test was carried using a sample of slightly increased thickness, and again known FVF of 60.5%. Fig. 10 shows the velocity as a function of propagation angle, generated from these data, and compared to the average and standard deviation limits provided by the 60.5% FVF calibration sample. The purpose of this step is to prove the validity of the method on different sample geometries and is impactful in that it clearly shows that the velocity as a function of

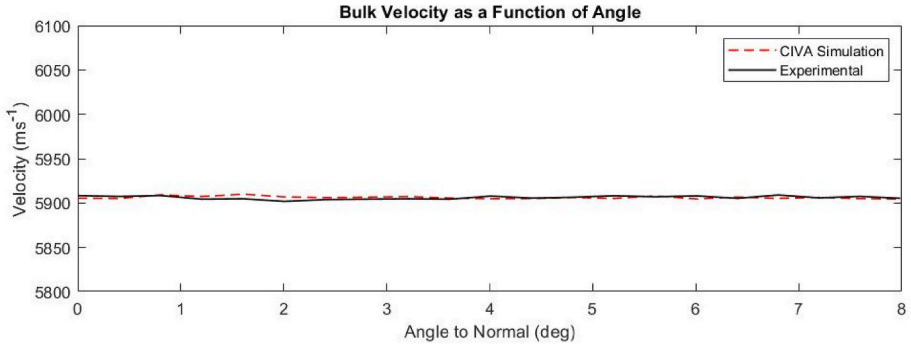

Fig. 7. Validation of method using FMC data acquired from a isotropic material, a glass calibration block. Experimental data and CIVA simulated data are plotted on the same axis.

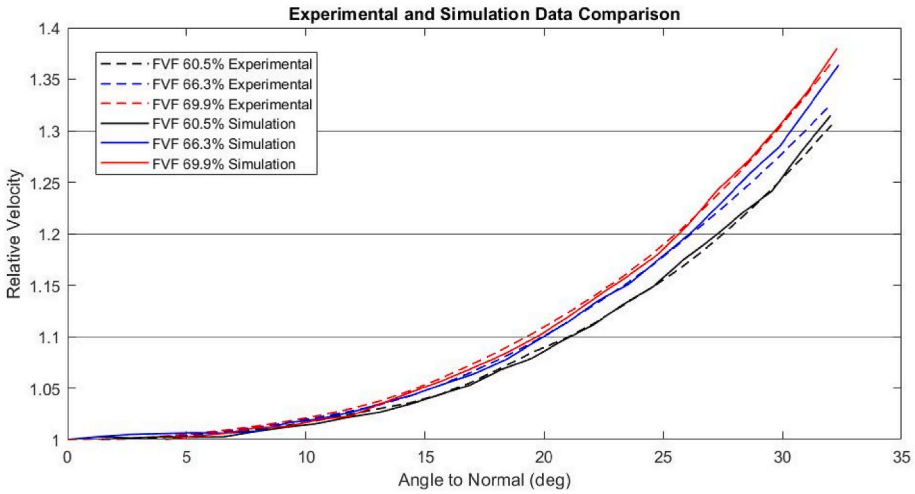

Fig. 8. Comparison of relative velocity as a function of angle to normal incidence. Three FVFs are plotted along with data from CIVA simulation. Velocity increase is normalised to that value observed at normal interface.

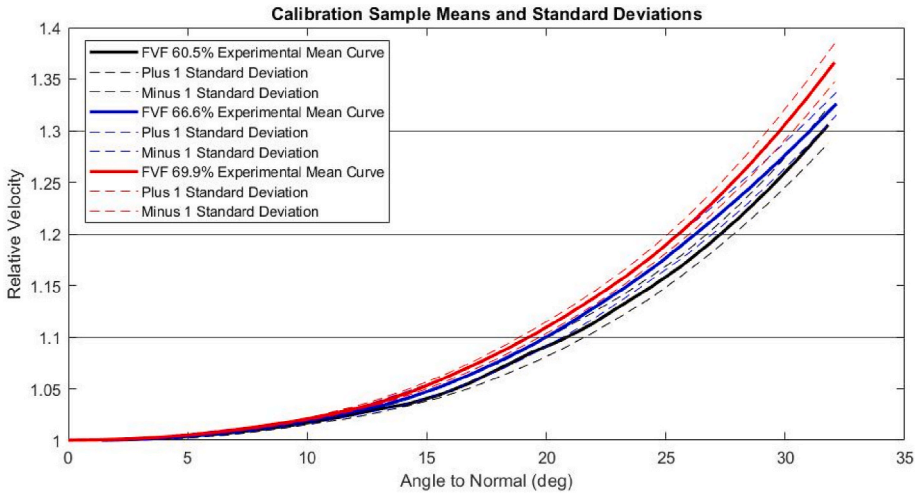

Fig. 9. Average curves generated for each FVF from the data presented in Fig. 8. Lower and upper screening curves are formed based on the standard deviation from the mean from highest and lowest FVF.

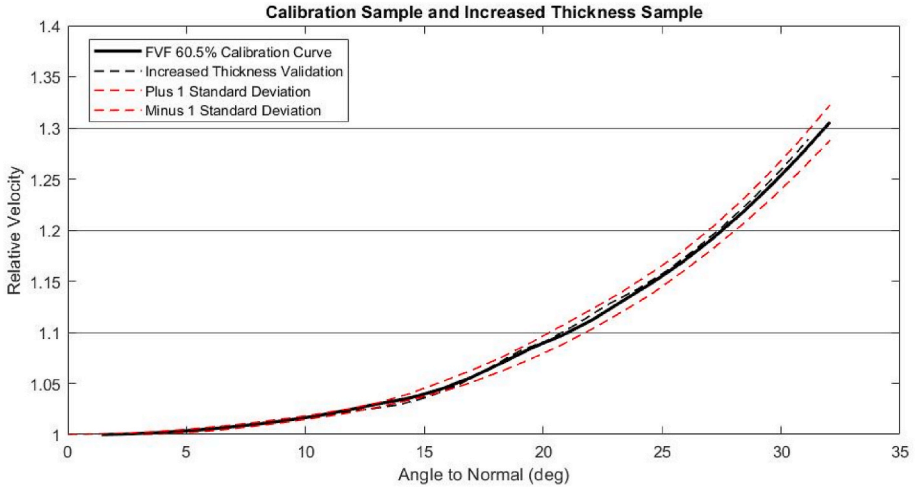

Fig. 10. Validation of method using FMC from a separate FVF 60.5% panel compared to the standard deviation as well as the FVF 60.5% calibration panel.

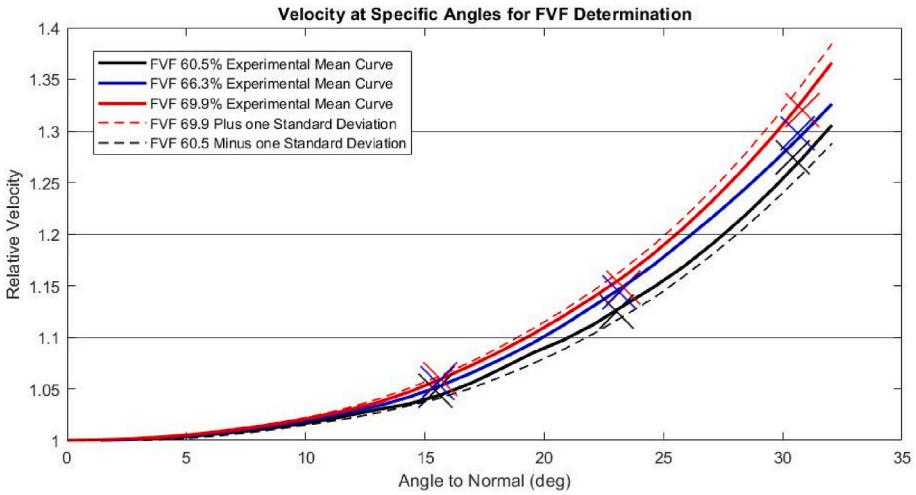

Fig. 11. Inspection implementation. Screening curves and average curves for each FVF calibration sample plotted alongside the point values of effective velocity increase at specific angles.

Table 2
Comparison of known and inspection FVF values alongside a percentage error.

Known FVF (%) (Acid digestion)	Interpolated FVF (%)	Percentage Error (%)
60.5	61.1	1.0
66.3	66.1	0.3
69.9	68.3	2.3

propagation angle is independent of sample thickness.

Mathematical theory presented and applied to CFRP panels of varying FVFs demonstrates, firstly the anisotropic nature of CFRP, in that the velocity changes with varying propagation angle, and secondly the extent by which this effect is influenced by the FVF. Thereby, ultrasonic velocity at varying propagation angles, proves to be a reliable method of distinguishing between FVF values. Lower FVF samples having a lower velocity, increasing more slowly as the propagation angle across the fibres steepens. Since the clear trend is only evident after averaging separate acquisitions at different locations on each sample the method is best suited as a screening process to ensure the FVF falls in the desired range of 60–70%, rather than a precise determination.

The effectiveness of the CIVA package is also clear when applied to composites. Using sample parameters such as the individual fibre thickness, density as well as sound velocity and density in the epoxy resin, CIVA can generate a highly accurate representation of the experimental composite. The results from each FVF model closely follow the curves generated experimentally. Again, any variation is due to experimental procedure and the accuracy with which the ToF between front and backwall echo can be measured using the sampling frequency. Sampling at 100 MHz is chosen so that the temporal position of front and back wall echo is known to an accuracy of 10^{-8} s giving an accuracy in the velocity of approximately 0.6% for the sample thickness of 5.1 mm.

When considering the range of angles across which the velocity is computed, attenuation becomes a key issue. Results presented here use a maximum gap between transmission and reception element of 25. Beyond this point, the amplitude of the back wall falls into the range of the noise floor. The minimal amplitude, received in a back wall reflection is shown in the following A-scans, Fig. 12, acquired using, first elements $T_{10}R_{15}$ and secondly $T_{10}R_{35}$. This results in a total angular variation of up to 31° based on the geometry of the inspection set-up, shown in Fig. 3 and using the numerical values given in Table 1.

In future, time-varying gain (TVG) could be applied to each A-scan to account for the increased attenuation of the back wall and the increased random noise. Also, a similar correction could be added when acquiring the FMC dataset. Higher gain values would be necessary, the further the acquisition shifts away from the FMC diagonal, where transmission and

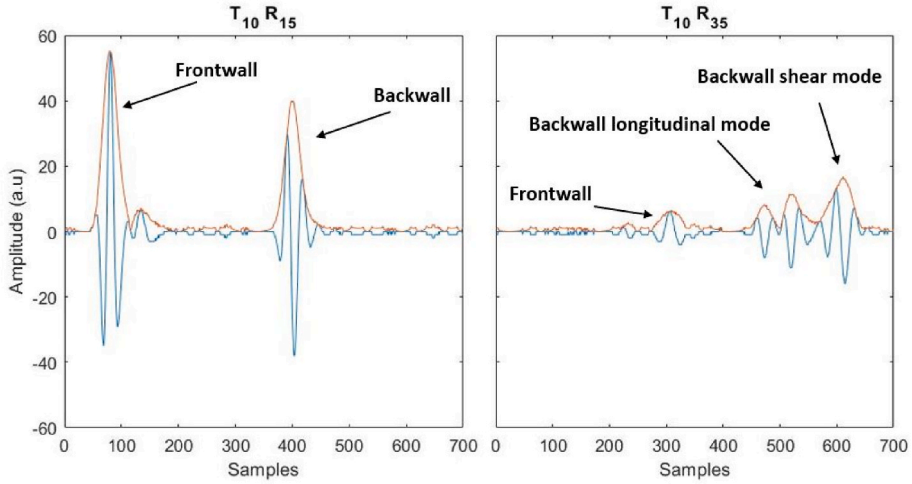

Fig. 12. Example A-scans from $T_{10}R_{15}$ and $T_{10}R_{35}$, highlighting the amplitude of echoes and thus the increased attenuation as propagation angle and distance are increased.

reception is on the same element. The sound will have to travel through a greater thickness of sample. The level of TVG necessary across a FMC dataset could also yield information on the FVF due to the variation in attenuation observed. Such steps would allow the propagation velocity curves, as a function of angle, to be extended beyond the values presented here.

6. Future work

Throughout the results and discussion sections, the effectiveness of the ray tracing model applied to FMC datasets, acquired through ultrasonic phased array testing, has been demonstrated. Therefore, the method presented here has been proven to be successful in FVF determination of pultruded CFRP panels. To further increase robustness as well as take steps to effectively incorporate the work into a manufacturing process, there are several avenues for future work.

To calculate the ray propagation angles in the model, the panel thickness must be obtained by manual measurement. This is currently performed using callipers and thus the accuracy is within 0.1 mm. It is not possible for ultrasonic determination of both thickness and velocity to be performed simultaneously. This would result in an algorithm input depending on the output with the velocity output influencing the initial thickness value. A possibility for future work would be for the thickness to be acquired from say, a 3D laser scanned model of the sample.

The inspection implementation has only been shown to give both accurate ultrasonic images and FVF determination when the phased array probe and sample are in a fixed position. Within a manufacturing environment, to characterise entire sections of sample, either the probe or sample would need to move so that 2D ultrasonic images can be generated alongside FVF determination. Whilst a commercially available phased array wheel probe is used for this work, bespoke wheel probes, and phased arrays, for a variety of NDT applications have been reported in Ref. [55]. These are an attractive option for future work since such a device could be custom designed to optimise both linear imaging, as well as FVF screening during inspection. Operation would require determination of the front and back wall peak location, robust enough to handle amplitude and ToF inconsistencies, stemming from probe movement. The longitudinal wave peak would still need to be reliably isolated from the shear wave ones when handling A-scans taken beyond the 1st critical angle. The method currently used for peak identification is not robust enough to handle data acquired from a moving probe and would therefore need to be refined.

7. Conclusions

A novel FVF screening technique based on analysis of a ray propagation model in combination FMC data, acquired from an ultrasonic phased array, has been presented. The validity of this is confirmed using both a isotropic glass block as well as simulation data from CIVA software using an additional composites package. The angular dependence of the sound velocity, with respect to the composite fibre direction, is shown to be a reliable parameter to distinguish between FVF values in the desired 60–70% range. Screening curves generated from calibration data are used to approximate the FVF of three separate datasets for validation. A discrepancy of no more that 2.3% in the worst case, and less than 1% in the best, is found between the known FVF values and those calculated using the methodology presented.

There is significant scope in terms of future work to allow the principles demonstrated to be reliably and robustly applied to a moving inspection and thereby integrated into a manufacturing environment. The benefit in the proposed form of FVF testing is multi-faceted. Firstly, there is value in the much faster results provided, as compared to conventional measurements. This remains valid even when precise ultrasonic measurement and the extensive data analysis procedures necessary, are considered. It is possible to produce more data, in a shorter period, for quality assurance. The non-destructive nature of ultrasonic measurement is also inherently safer for operators. Finally, a lower cost of testing is achieved due to the significantly shortened preparation and test time. Results shown are beneficial to the manufacturing process with the potential to ensure that final components satisfy manufacturing standards and are a powerful tool in guaranteeing that FVF consistency is maintained.

Author statement

Euan Duernberger: Conceptualization, methodology, data curation, writing, original draft preparation, reviewing and editing, **Charles MacLeod**: Supervision, reviewing and editing, methodology, **Dave Lines:** Methodology, reviewing.

Declaration of competing interest

The authors declare that they have no known competing financial interests or personal relationships that could have appeared to influence the work reported in this paper.

Data availability

Data will be made available on request.

Acknowledgement

The author acknowledges the funding of the Engineering and Physical Sciences Research Council (EPSRC), supplied through the Centre for Doctoral Training in Wind and Marine Energy Systems, in making this research possible.

References

[1] Rajak DK, Pagar DD, Kumar R, Pruncu CI. Recent progress of reinforcement materials: a comprehensive overview of composite materials. J Mater Res Technol 2019;8(6):6354–74. https://doi.org/10.1016/j.jmrt.2019.09.068.
[2] Shue B, Moreira A, Flowers G. Review of recent developments in composite material for aerospace applications. Proc. ASME Des. Eng. Tech. Conf. 2009;1:811–9. https://doi.org/10.1115/DETC2009-87847. PARTS A AND B.
[3] Li C, Pain D, Wilcox PD, Drinkwater BW. Imaging composite material using ultrasonic arrays. NDT E Int 2013;53:8–17. https://doi.org/10.1016/j.ndteint.2012.07.006.
[4] Fuentes R, et al. Autonomous ultrasonic inspection using Bayesian optimisation and robust outlier analysis. Mech Syst Signal Process 2020;145:106897. https://doi.org/10.1016/j.ymssp.2020.106897.
[5] Wang B, Zhong S, Lee TL, Fancey KS, Mi J. Non-destructive testing and evaluation of composite materials/structures: a state-of-the-art review. Adv Mech Eng 2020;12(4):1–28. https://doi.org/10.1177/1687814020913761.
[6] Lee J, Zhao F. Gobal wind report 2021. Glob. Wind Energy Counc.; 2021. p. 75.
[7] O. for N. Statistics. Wind energy in the UK. 2021.
[8] WindEurope. Offshore wind in europe: key trends and statistics. 2020.
[9] RenewableCube wind. 2021.
[10] Deng XW, Wu N, Yang K, Chan WL. Integrated design framework of next-generation 85-m wind turbine blade: modelling, aeroelasticity and optimization. Compos B Eng 2019;159:53–61. https://doi.org/10.1016/j.compositesb.2018.09.028. August 2018.
[11] SG 8.0-167 DD. Product brochure." Siemens Gamesa Renewable Energy, pp. 1–2.
[12] Siemens Gamesa launches 10 MW offshore wind turbine. SGRE Newsroom; 2019.
[13] Bender JJ, Hallett SR, Lindgaard E. Investigation of the effect of wrinkle features on wind turbine blade sub-structure strength. Compos Struct 2019;218:39–49. https://doi.org/10.1016/j.compstruct.2019.03.026.
[14] Colombi P, Poggi C. An experimental, analytical and numerical study of the static behavior of steel beams reinforced by pultruded CFRP strips. Compos B Eng 2006;37(1):64–73. https://doi.org/10.1016/j.compositesb.2005.03.002.
[15] Ali MI, Anjaneyulu J. Effect of fiber-matrix volume fraction and fiber orientation on the design of composite suspension system. IOP Conf Ser Mater Sci Eng 2018;455(1). https://doi.org/10.1088/1757-899X/455/1/012104.
[16] Wang Q, Ning H, Vaidya U, Pillay S, Nolen LA. Development of a carbonization-in-nitrogen method for measuring the fiber content of carbon fiber reinforced thermoset composites. Compos Appl Sci Manuf 2015;73:80–4. https://doi.org/10.1016/j.compositesa.2015.02.025.
[17] Kim H, Kim G, Lee S, Choe G, Noguchi T, Nam J. Direct tensile behavior of amorphous metallic fiber-reinforced cementitious composites: effect of fiber length, fiber volume fraction, and strain rate. Compos B Eng 2019;177:107430. https://doi.org/10.1016/j.compositesb.2019.107430. July.

[18] Chen JH, Schulz E, Bohse J, Hinrichsen G. Effect of fibre content on the interlaminar fracture toughness of unidirectional glass-fibre/polyamide composite. Compos. Part A Appl Sci Manuf 1999;30(6):747–55. https://doi.org/10.1016/S1359-835X(98)00188-2.
[19] Okoli OI, Smith GF. Failure modes of fibre reinforced composites: the effects of strain rate and fibre content. J Mater Sci 1998;33(22):5415–22. https://doi.org/10.1023/A:1004406618845.
[20] Belmonte E, De Monte M, Hoffmann CJ, Quaresimin M. Damage initiation and evolution in short fiber reinforced polyamide under fatigue loading: influence of fiber volume fraction. Compos B Eng 2017;113:331–41. https://doi.org/10.1016/j.compositesb.2017.01.023.
[21] Kardos M, Körner E, Penumadu D, Modler N. The influence of fiber volume fraction and fiber length on the evolution of pore content and the paintability of sheet molding compounds. Compos B Eng 2020;185:107760. https://doi.org/10.1016/j.compositesb.2020.107760. January.
[22] Esnaola A, Tena I, Aurrekoetxea J, Gallego I, Ulacia I. Effect of fibre volume fraction on energy absorption capabilities of E-glass/polyester automotive crash structures. Compos B Eng 2016;85:1–7. https://doi.org/10.1016/j.compositesb.2015.09.007.
[23] Abdalla F, Megat M, Sapuan M, Bb S. Determination of volume fraction values of filament wound glass and carbon fiber reinforced composites. ARPN J Eng Appl Sci 2008;3(4):7–11.
[24] Grund D, Orlishausen M, Taha I. Determination of fiber volume fraction of carbon fiber-reinforced polymer using thermogravimetric methods. Polym Test 2019;75:358–66. https://doi.org/10.1016/j.polymertesting.2019.02.031. March.
[25] Mohsin MAA, Iannucci L, Greenhalgh ES. Fibre-volume-fraction measurement of carbon fibre reinforced thermoplastic composites using thermogravimetric analysis. Heliyon 2019;5(1):e01132. https://doi.org/10.1016/j.heliyon.2019.e01132.
[26] ASTM D3171-22. Standard test methods for constituent content of composite materials. 2012.
[27] Cilley E, Roylance D, N S. Methods of fibre and void measurement in graphite epoxy composites. 1974.
[28] Waterbury MC, Drzal LT. Determination of fiber volume fractions by optical numeric volume fraction analysis. J Reinforc Plast Compos 1989;8(6):627–36. https://doi.org/10.1177/073168448900800605.
[29] He HW, Huang W, Gao F. Comparison of four methods for determining fiber content of carbon fiber/epoxy composites. Int J Polym Anal Char 2016;21(3):251–8. https://doi.org/10.1080/1023666X.2016.1139395.
[30] Zbončák R, Votrubec V, Švec M. The alternative procedures of fiber volume ratio determination of long-fiber carbon - epoxy composites. Manuf. Technol. 2018;18(1):160–4. https://doi.org/10.21062/ujep/71.2018/a/1213-2489/MT/18/1/160.
[31] Krautkramer J, Krautkramer H. Ultrasonic testing of materials. 1990.
[32] Ghobadi A. Common type of damages in composites and their inspections. World J Mech 2017:24–33. https://doi.org/10.4236/wjm.2017.72003. 07, no. 02.
[33] Gholizadeh S. A review of non-destructive testing methods of composite materials. Procedia Struct Integr 2016;1:50–7. https://doi.org/10.1016/j.prostr.2016.02.008.
[34] García Márquez FP, Peco Chacón AM. A review of non-destructive testing on wind turbines blades. Renew Energy 2020;161:998–1010. https://doi.org/10.1016/j.renene.2020.07.145.
[35] Amenabar I, Mendikute A, López-Arraiza A, Lizaranzu M, Aurrekoetxea J. Comparison and analysis of non-destructive testing techniques suitable for delamination inspection in wind turbine blades. Compos B Eng 2011;42(5):1298–305. https://doi.org/10.1016/j.compositesb.2011.01.025.
[36] Kažys R, Tumšys O, Pagodinas D. Ultrasonic detection of defects in strongly attenuating structures using the Hilbert-Huang transform. NDT E Int 2008;41(6):457–66. https://doi.org/10.1016/j.ndteint.2008.03.006.
[37] Tiwari KA, Raisutis R. Post-processing of ultrasonic signals for the analysis of defects in wind turbine blade using guided waves. J Strain Anal Eng Des 2018;53(8):546–55. https://doi.org/10.1177/0309324718772668.
[38] BINDT. Report from the workshop on NDT and SHM requirements for wind turbines. Rep. from Work. NDT SHM Requir. *Wind Turbines* 2019. February.
[39] Yang R, He Y, Zhang H. Progress and trends in nondestructive testing and evaluation for wind turbine composite blade. Renew Sustain Energy Rev 2016;60:1225–50. https://doi.org/10.1016/j.rser.2016.02.026.
[40] Du Y, Zhou S, Jing X, Peng Y, Wu H, Kwok N. Damage detection techniques for wind turbine blades: a review. Mech Syst Signal Process 2020;141:106445. https://doi.org/10.1016/j.ymssp.2019.106445.
[41] Séguin-Charbonneau L, Walter J, Théroux LD, Scheed L, Beausoleil A, Masson B. Automated defect detection for ultrasonic inspection of CFRP aircraft components. NDT E Int 2021;122. https://doi.org/10.1016/j.ndteint.2021.102478. February.
[42] Drinkwater BW, Wilcox PD. Ultrasonic arrays for non-destructive evaluation: a review. NDT E Int 2006;39(7):525–41. https://doi.org/10.1016/j.ndteint.2006.03.006.
[43] Mohammadkhani R, Fragonara LZ, Janardhan PM, Petrunin I, Tsourdos A, Gray I. Ultrasonic phased array imaging technology for the inspection of aerospace composite structures. In: 2019 IEEE int. Work. Metrol. AeroSpace, Metroaerosp. 2019 - Proc.; 2019. p. 203–8. https://doi.org/10.1109/MetroAeroSpace.2019.8869635.
[44] Holmes C, Drinkwater BW, Wilcox PD. Post-processing of the full matrix of ultrasonic transmit-receive array data for non-destructive evaluation. NDT E Int 2005;38(8):701–11. https://doi.org/10.1016/j.ndteint.2005.04.002.
[45] Zhang J, Drinkwater BW, Wilcox PD. Comparison of ultrasonic array imaging algorithms for non-destructive evaluation. AIP Conf Proc 2013;1511(8):825–32. https://doi.org/10.1063/1.4789130.
[46] Ménard C, Robert S, Miorelli R, Lesselier D. Optimization algorithms for ultrasonic array imaging in homogeneous anisotropic steel components with unknown properties. NDT E Int 2020;116. https://doi.org/10.1016/j.ndteint.2020.102327.
[47] Cao H, Guo S, Zhang S, Xie Y, Feng W. Ray tracing method for ultrasonic array imaging of CFRP corner part using homogenization method. NDT E Int 2021;122:102493. https://doi.org/10.1016/j.ndteint.2021.102493. June.
[48] Fan Z, Mark AF, Lowe MJS, Withers PJ. Nonintrusive estimation of anisotropic stiffness maps of heterogeneous steel welds for the improvement of ultrasonic array inspection. IEEE Trans Ultrason Ferroelectrics Freq Control 2015;62(8):1530–43. https://doi.org/10.1109/TUFFC.2015.007018.
[49] Education IT. Single crystal turbine blade inspection using a 2D ultrasonic array. 2004. p. 1–7. 50239030.
[50] Kusano M, Takizawa S, Sakai T, Arao Y, Kubouchi M. Simultaneous sound velocity and thickness measurement by the ultrasonic pitch-catch method for corrosion-layer-forming polymeric materials. Ultrasonics 2018;82:178–87. https://doi.org/10.1016/j.ultras.2017.08.001.
[51] [Online]. Available: IMA dresden https://www.ima-dresden.de/.
[52] Mineo C, et al. Flexible integration of robotics, ultrasonics and metrology for the inspection of aerospace components. AIP Conf Proc 2017;1806. https://doi.org/10.1063/1.4974567. February.
[53] Mineo C, et al. Fast ultrasonic phased array inspection of complex geometries delivered through robotic manipulators and high speed data acquisition instrumentation. IEEE Int. Ultrason. Symp. IUS 2016:1–4. https://doi.org/10.1109/ULTSYM.2016.7728746. 2016-Novem.
[54] CIVA NDE. CIVA 2020 user manual," no. CIVA NDE; 2020. p. 1000.
[55] Vithanage RKW, et al. A phased array ultrasound roller probe for automated in-process/interpass inspection of multipass welds. IEEE Trans Ind Electron 2021;68(12):12781–90. https://doi.org/10.1109/TIE.2020.3042112.